

Development of mitigation strategies for process-induced deformations through finite elements

*Original*

Development of mitigation strategies for process-induced deformations through finite elements / Zappino, E.; Masia, R.; Zobeiry, N.; Petrolo, M.; Carrera, E.. - In: MECHANICS OF ADVANCED MATERIALS AND STRUCTURES. - ISSN 1537-6494. - ELETTRONICO. - 31:28(2024), pp. 11054-11066. [10.1080/15376494.2024.2343326]

*Availability:*

This version is available at: 11583/2995200 since: 2024-12-11T15:21:25Z

*Publisher:*

Taylor & Francis

*Published*

DOI:10.1080/15376494.2024.2343326

*Terms of use:*

This article is made available under terms and conditions as specified in the corresponding bibliographic description in the repository

*Publisher copyright*

Taylor and Francis postprint/Author's Accepted Manuscript con licenza CC by-nc-nd

This is an Accepted Manuscript version of the following article: Development of mitigation strategies for process-induced deformations through finite elements / Zappino, E.; Masia, R.; Zobeiry, N.; Petrolo, M.; Carrera, E.. - In: MECHANICS OF ADVANCED MATERIALS AND STRUCTURES. - ISSN 1537-6494. - ELETTRONICO. - 31:28(2024), pp. 11054-11066. [10.1080/15376494.2024.2343326]. It is deposited under

(Article begins on next page)

# Development of mitigation strategies for process-induced deformations through finite elements

E. Zappino<sup>1,\*</sup>, R. Masia<sup>1,†</sup>, N. Zobeiry<sup>2,‡</sup>, M. Petrolo<sup>1,§</sup>, E. Carrera<sup>1,¶</sup>

<sup>1</sup> Mul2 Lab, Department of Mechanical and Aerospace Engineering, Politecnico di Torino  
Torino, Italy.

<sup>2</sup> Materials Science & Engineering Department, University of Washington, Seattle, USA.

Revised version of manuscript ID 241969279

*Author for correspondence:*

Marco Petrolo

MUL<sup>2</sup> Lab, Department of Mechanical and Aerospace Engineering,

Politecnico di Torino,

Corso Duca degli Abruzzi 24,

10129 Torino, Italy,

tel: +39 011 090 6845,

e-mail: marco.petrolo@polito.it

---

\*E-mail: enrico.zappino@polito.it

†E-mail: rebecca.masia@polito.it

‡E-mail: navidz@uw.edu

§E-mail: marco.petrolo@polito.it

¶E-mail: erasmo.carrera@polito.it

**Abstract:** *The present work investigates the residual deformations arising from the curing process of composite curved parts and mitigation strategies to reduce them. Numerical simulations based on finite elements and refined structural theories are adopted and verified against closed-form solutions. The higher-order structural theories are based on the Carrera Unified Formulation, and one-dimensional models are built using layer-wise kinematics. The Cure-Hardening Instantaneously Linear Elastic constitutive model is used. The analytical formulation includes the effects of the final demolding and the in-plane deformations. Results consider spring-in and warping angles after the tool removal. The numerical efficiency of the one-dimensional model allows for thorough parametric analyses, and all the possible combinations of an eight-layer cross-ply laminate are considered. The results confirm that the in-plane deformation and the final demolding play a fundamental role in process-induced deformations. Furthermore, deformations can be significantly reduced by considering asymmetric laminates and localized composite patches.*

**Keywords:** Curing; virtual manufacturing; composites; CUF; process-induced deformations

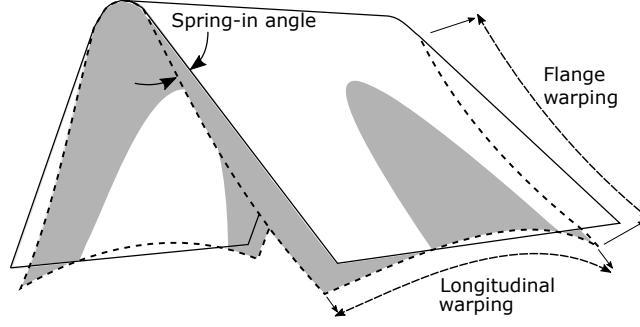


Figure 1: Spring-in angle and warping phenomenon in a L-shaped model.

## 1 Introduction

Fiber-reinforced polymer composites have become increasingly popular in aerospace applications due to their high strength-to-weight ratio and excellent fatigue resistance. The autoclave processing method [1] is the most commonly used manufacturing technique for high-performance composite materials. The autoclave facilitates the removal of trapped air or moisture by using high pressures and temperature cycles to activate the resin and cure the material.

The autoclave process can induce residual stresses and strains within the composite material [2], deriving from many factors, e.g., the thermal expansion mismatch between the fiber and the resin matrix and the shrinkage [3]. These defects may be critical for the final shape of the cured part and can affect the structure's performance. Therefore, minimizing such defects and residual stresses is desirable [4].

The Process Induced Deformations (PID) can be seen as combining the spring-in angle and the warpage. In the case of curved parts, such as the well-known L-shaped parts, the spring-in angle refers to the deviation of a part's angle from its nominal value, which occurs when the part is removed from the mold after curing. On the other hand, warpage refers to the change in curvature both in the longitudinal direction and along the flange after it has been manufactured, as shown in Fig. 1. Due to the intrinsic multiscale nature of composite materials, residual stresses can cause different issues depending on the scale of interest. For instance, residual stresses may lead to critical shape distortion at the laminate level. On the other hand, at the micro-scale level, the structure can experience micro-cracks or fiber-matrix debonding [5, 6, 7]. Multiple factors can influence the extent of deformation, such as the materials, the stacking sequence, part geometry, and curing cycle type. Classifying the known parameters that may affect spring-in angle [8] as intrinsic or extrinsic is convenient. Intrinsic parameters are defined as parameters related to part geometry and material properties, whereas extrinsic parameters are related to tooling and processing. In a recent work by Traiforos et al. [9], the authors concluded that the material of the tool has a significant effect on the final spring-in angle and also that a fast curing cycle leads to a higher spring-in angle. Thus, a comprehensive investigation of the combined effect of these parameters is necessary. Many works on experimental and numerical activities have recently been published [10, 11]. Carolynne and Fernlund [12] show that both design and process parameters affect spring-in and warpage and demonstrate that spring-in of curved laminates is sensitive to the measurement technique. Thinner parts have

greater spring-in values than thicker [13]. Notably, among all the parameters that could be manipulated to manage the final spring-in angle, the stacking sequences of the component strongly impact the result [14]. Sorrentino and Bellini [15] found that higher values of thickness reduction minimize residual stresses for the composite structures with angled cross-sections. Moreover, in the work of Zhang et al., [16], a parametric study was conducted to investigate the influence of the corner radius, the fiber orientation, the laminate thickness, and the flange length on the spring-in angle of variable-stiffness components using commercial numerical tools. More recently, many studies have proposed combined methods based on experiments, simulations, and machine learning to investigate the effect of processing variables and the experimental conditions [17, 18, 19]. Analytical methods are commonly used as they provide results quickly and are helpful for benchmarking analyses. In [20], an analytical solution for spring-in angles of curved composites is presented. Ding et al. [21] proposed an analytical solution considering the effect of the flange on spring-in angles in L-shaped parts. Additionally, in [22], a parametric study is presented to investigate the influence of curing cycle, geometry, tool thermal expansion, and resin characteristics on PID. Takagaki et al. [23] proposed a novel analytical method for L-shaped parts to evaluate the residual spring-in angles. In the work of Balaji et al., [24], advanced rheological models and neural networks are integrated into finite element modeling to improve predictions of distortions during thermoset polymerization processes markedly.

In recent years, research works on mitigation strategies have been published. In the work of Zobeiry and Pour-sartip [2], three methods are employed to mitigate the effects of residual stresses and deformations: design compensation, assembly compensation, and mold geometry compensation. The latter is preferred as it involves predicting the deformed geometry of the part using process simulation tools and compensating the mold geometry accordingly, ensuring parts with geometric deviations within design tolerances can be manufactured. Other recent works propose alternative methods for introducing prestress to a single layer or part of the layers [25]. Moreover, the work [8] presents the process optimization strategies for minimizing the PID during manufacture, and Wucher [26] proposed mold compensation approaches.

Since residual deformations develop mainly through thickness, using a numerical model that includes through-the-thickness deformation is essential. Thus, within this work, a numerical simulation technique based on the Carrera Unified Formulation (CUF) [27, 28, 29] and the Finite Element Method (FEM) is employed. The CUF enables a higher-order one-dimensional model, which accurately describes the three-dimensional response of the structure, thus significantly reducing computational costs and accelerating simulation times compared to more complex 3D simulations [30]. Using Layer-Wise (LW) models becomes necessary to precisely predict the residual deformations [31, 32]. The present work focuses on exploiting the computational efficiency of CUF to investigate the effect of stacking sequences on PID and introducing innovative mitigation strategies. In addition, the results are compared to an analytical formulation based on [23], and new effects are incorporated into the former formulation.

The present paper is organized as follows: Section 2 presents the one-dimensional refined model based on CUF

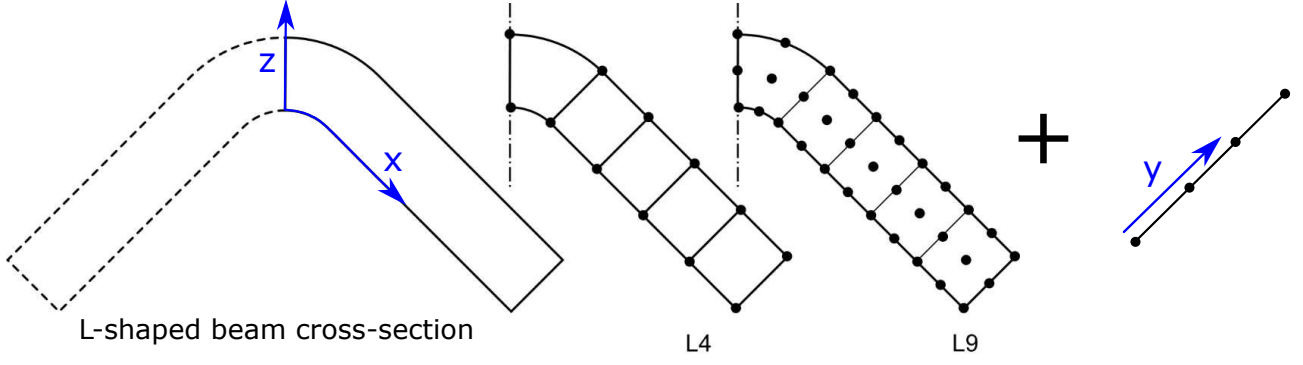


Figure 2: Beam model of the L-shaped part with its coordinate system and the discretization of the cross-section using L4 and L9.

and its capabilities. Then, in Section 3, the curing process and the L-shaped model are described. Section 4 reports the closed-form solution used in the verification process. Furthermore, Section 5 assesses the present numerical model against analytical solutions. In Section 6.1, numerical results are presented for symmetric and asymmetric laminations, and the mitigation of the predicted residual deformations is discussed. The paper's main results are summarized and discussed in Section 7. Finally, Section 8 presents conclusions and perspectives.

## 2 CUF one-dimensional theories for virtual manufacturing

The numerical approach adopted in this study is based on the well-established Carrera Unified Formulation (CUF) to develop higher-order structural theories, which provides a level of accuracy comparable to three-dimensional (3D) models while ensuring lower computational costs [27, 33]. According to CUF, the governing equations can be expressed in a compact form, which remains independent of the structural theory adopted; in the case of finite elements (FE) and according to the reference system in Fig. 2, the 3D three-dimensional displacement field can be reduced to a 1D modeling as follows:

$$\mathbf{u}(x, y, z) = F_\tau(x, z)N_i(y)\mathbf{u}_{\tau i} \quad \tau = 1, \dots, M \quad i = 1, \dots, N_n \quad (1)$$

where  $F_\tau(x, z)$  is the expansion function defining the structural theory cross-section direction,  $N_i(y)$  is the shape function employed along the beam direction, and  $\mathbf{u}_{\tau i}$  are the nodal unknowns. Furthermore,  $M$  is the number of the expansion function terms, and  $N_n$  is the number of the 1D element nodes. The expansion functions in the present analysis are based on Lagrange polynomials, leading to a Layer-Wise (LW) approach, where each layer of the laminate has its own set of displacement variables. In Fig. 2, linear four-node (L4) and quadratic nine-node (L9) Lagrange elements over the cross-section of the model are shown. In the results section, a convergence analysis will be conducted to choose elements among those presented. The displacement field with

L9 elements becomes [34]:

$$\begin{aligned}
u_x &= L_1 u_{x1} + L_2 u_{x2} + L_3 u_{x3} + L_4 u_{x4} + L_5 u_{x5} + L_6 u_{x6} + L_7 u_{x7} + L_8 u_{x8} + L_9 u_{x9} \\
u_y &= L_1 u_{y1} + L_2 u_{y2} + L_3 u_{y3} + L_4 u_{y4} + L_5 u_{y5} + L_6 u_{y6} + L_7 u_{y7} + L_8 u_{y8} + L_9 u_{y9} \\
u_z &= L_1 u_{z1} + L_2 u_{z2} + L_3 u_{z3} + L_4 u_{z4} + L_5 u_{z5} + L_6 u_{z6} + L_7 u_{z7} + L_8 u_{z8} + L_9 u_{z9}
\end{aligned} \tag{2}$$

where L denotes the use of Lagrange functions, on the other hand, over the beam y-direction, cubic four-node elements (B4) are employed, as shown in Fig. 2.

The stress and strain fields are expressed as follows:

$$\begin{aligned}
\boldsymbol{\varepsilon}^T &= \{\varepsilon_{xx}, \varepsilon_{yy}, \varepsilon_{zz}, \varepsilon_{xz}, \varepsilon_{yz}, \varepsilon_{xy}\} \\
\boldsymbol{\sigma}^T &= \{\sigma_{xx}, \sigma_{yy}, \sigma_{zz}, \sigma_{xz}, \sigma_{yz}, \sigma_{xy}\}
\end{aligned} \tag{3}$$

The displacement-strain geometrical relation is given by:

$$\boldsymbol{\varepsilon} = \mathbf{D}\mathbf{u} \tag{4}$$

where  $\mathbf{D}$  is a  $6 \times 3$  linear differential operator [27]. The stress-strain constitutive relation is

$$\boldsymbol{\sigma} = \mathbf{C}\boldsymbol{\varepsilon} \tag{5}$$

where  $\mathbf{C}$  is the material coefficient matrix. The Principle of Virtual Displacements (PVD) is used for the governing equations,

$$\delta L_{int} = \delta L_{ext} \tag{6}$$

where  $\delta L_{int}$  is the variation of the internal work, and  $\delta L_{ext}$  the variation of the work from the external forces. The internal work in Eq. (6) is formulated through the constitutive equations from Eq. (5) and the geometrical relations from Eq. (4):

$$\delta L_{int} = \int_V \delta \boldsymbol{\varepsilon}^T \boldsymbol{\sigma} dV = \delta \mathbf{u}_{sj}^T \underbrace{\int_V [N_j F_s \mathbf{D}^T \mathbf{C} \mathbf{D} F_\tau N_i] dV}_{\mathbf{k}^{ij\tau s}} \mathbf{u}_{\tau i} = \delta \mathbf{u}_{sj}^T \mathbf{k}^{ij\tau s} \mathbf{u}_{\tau i} \tag{7}$$

where  $\mathbf{u}_{\tau i}$  are the nodal unknowns and  $\delta \mathbf{u}_{sj}^T$  their variations. The  $3 \times 3$  fundamental nucleus of the problem,  $\mathbf{k}^{ij\tau s}$ , is then assembled over the four indices i, j,  $\tau$ , s to obtain the overall stiffness matrix  $\mathbf{K}$ .

Assuming that the external load arises from thermal and chemical fields generated during the curing process, the work of the external forces can be expressed as the sum of two distinct contributions:

$$\delta L_{ext} = \int_V \delta \boldsymbol{\varepsilon}^T \mathbf{C} \boldsymbol{\alpha} \Delta T dV + \int_V \delta \boldsymbol{\varepsilon}^T \mathbf{C} \boldsymbol{\varepsilon}_S dV \tag{8}$$

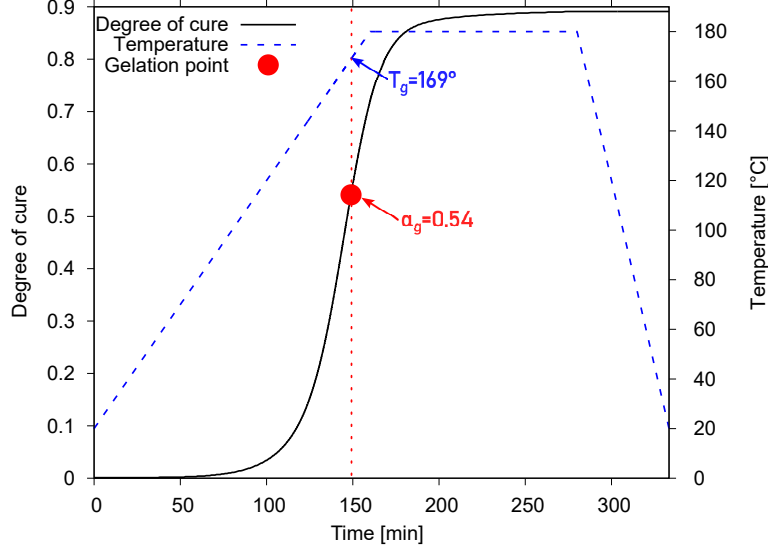


Figure 3: Evolution of degree of cure and temperature of the curing cycle.

where  $\alpha\Delta T$  is the deformation related to the thermal field,  $\alpha$  is the coefficient of thermal expansion vector,  $\Delta T$  is the temperature variation, and  $\varepsilon_S$  is related to the chemical shrinkage. Therefore, the external work in the CUF framework becomes

$$\delta L_{ext} = \delta \mathbf{u}_{sj}^T \underbrace{\int_V N_j F_s \mathbf{D}^T \mathbf{C}}_{\mathbf{f}^{js}} (\alpha \Delta T + \varepsilon_S) dV = \delta \mathbf{u}_{sj}^T \mathbf{f}^{js} \quad (9)$$

where  $\mathbf{f}^{js}$  is the  $1 \times 3$  fundamental nucleus of the load vector, assembled over the indices  $j$  and  $s$  provides the global load vector  $\mathbf{F}$ .

The numerical simulation employed in this investigation is based on the Cure-Hardening Instantaneously Linear Elastic (CHILE) constitutive model, described in [35]. This model is used for the monotonic evolution of the composite's elastic properties during the progression of the cure. The CHILE model assumes the material exhibits an instantaneous linear elastic response, although the elastic constants may vary throughout the simulation. The solution at the end of the process is the cumulative summation of the incremental elastic solutions corresponding to each individual  $t_i$ -th step [32],

$$\mathbf{u} = \sum_{t_i=1}^{N_\alpha} \Delta \mathbf{u}_{t_i} \quad (10)$$

where  $t_i$  is the current step and  $N_\alpha$  is the total number of steps. The simulation of the curing process starts at the gelation point [1], indicated by the degree of cure  $\alpha_g$  and the gelation temperature  $T_g$  in Fig. 3. The elastic properties are updated at each time step, and the incremental deformations resulting from the thermal effect  $\Delta \varepsilon_T^{t_i}$  and the chemical effect  $\Delta \varepsilon_S^{t_i}$  are considered in the calculation of the external load. The incremental



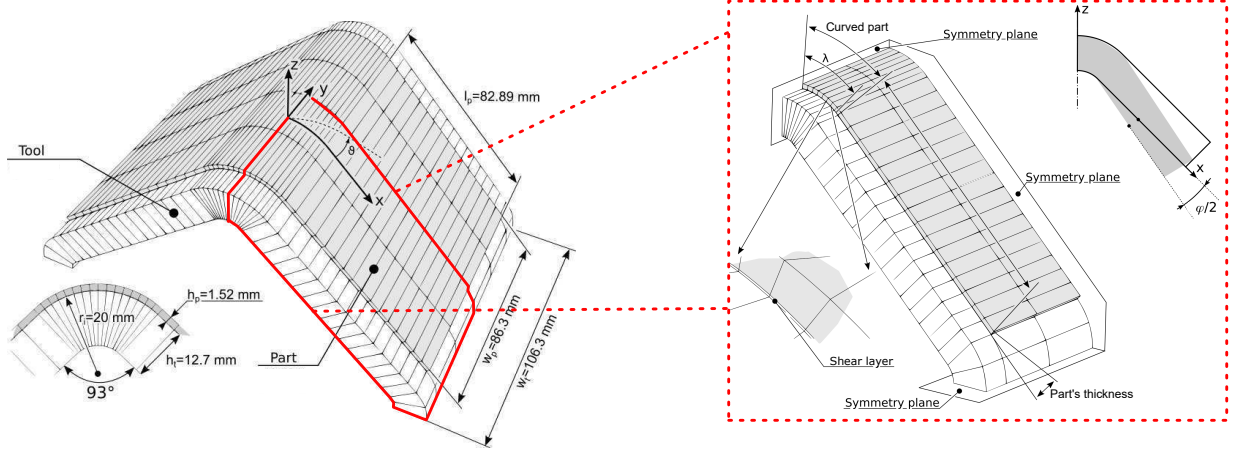


Figure 4: Geometry of the L-shaped component on the tool and applied boundary conditions.

contribution at each step is computed as

$$\Delta \mathbf{u}_{t_i} = [\mathbf{K}]_{t_i}^{-1} \Delta \mathbf{F}_{t_i} \quad (11)$$

where  $[\mathbf{K}]_{t_i}$  is the stiffness matrix combining the part, the tool, and the shear layer at the  $i$ -th step;  $\Delta \mathbf{F}_{t_i}$  is the variation of the global forces. More details about the simulation procedure are in [32]. The analysis conducted in the present work is linear.

### 3 L-shape part, material properties, and curing cycle

This section describes the L-shaped model, including the features related to the geometry adopted in the numerical analysis, as shown in Fig. 4. The component comprises eight plies, each with a thickness of 0.19 mm - for a total thickness of 1.52 mm - and balanced/unbalanced cross-ply laminations and symmetric/asymmetric stackings, as detailed in the result section. The lamination angle, denoted as  $\theta$ , is defined relative to  $x$ . Consequently, for a lamination with  $\theta = 90^\circ$ , the fibers are parallel to  $y$ . Due to the symmetry of the model in both geometry and loading conditions, only the portion highlighted on the right side of Fig. 4 is modeled; three symmetries are imposed: two are related to the composite part on the  $x$ - $z$  and  $y$ - $z$  planes, and the third pertains to the tool, on the  $x$ - $y$  plane. Moreover, the interaction between the tool and the part is modeled as frictionless, adopting a reduced shear stiffness to allow relative sliding. Thus, the tool-part interaction [36] is not considered in the present paper.

The composite material adopted is the AS4/8552 unidirectional prepreg from Hexcel. The cured ply of this prepreg has a thickness of approximately 0.19 mm and is composed of about 35% 8552 epoxy resin by weight [37] and 65% AS4 HexTow carbon fibers with an aerial weight of 190gsm [38] [39, 40]. The tool's material and the shear layer is the Invar, with  $E = 150$  GPa,  $\nu = 0.28$ ,  $\alpha = 1.56 \times 10^{-6}$  / $^\circ\text{C}$ . The RAVEN Software [41] supplied the data related to the curing process and the progression of mechanical properties. The 8552 free-strains from [42] have been incorporated into the RAVEN simulation. The curing cycle is reported in Fig.

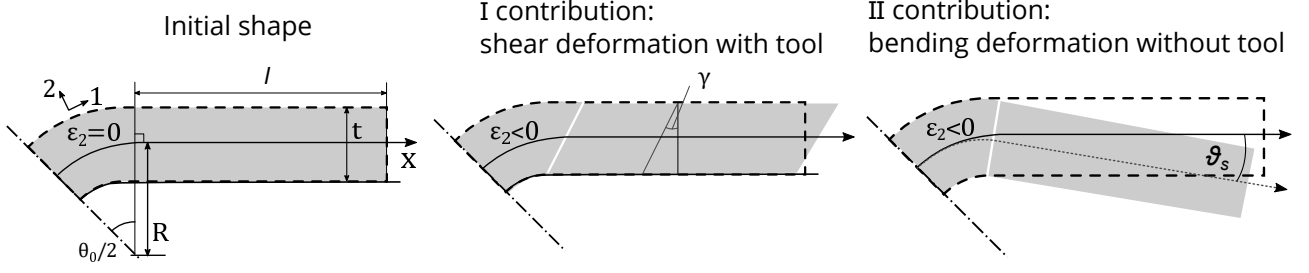


Figure 5: L-shaped model in its original state (left) alongside the two deformation contributions in the closed-form solution.

3, featuring a heating rate of  $1^\circ\text{C}/\text{min}$ , followed by a hold temperature at  $180^\circ\text{C}$  for 120 minutes, and a final cool-down step, leading to a total cycle duration of approximately 333 minutes. All the material properties are available in [32].

## 4 Closed-form solutions for process induced deformations of L-shaped parts

In the following section, the closed-form solution involved in assessing the numerical analysis is presented. The analytical model is based on the work of Takagaki et al. [23] and considers an L-shaped component comprised of two separate parts: the C-shaped part proposed by [43] and the flange. The model and coordinate system are shown in Fig. 5. The closed-form solution considers the in-plane direction, 1, and the through-the-thickness direction, 2. Similarly to the numerical model, only half of the L-shaped laminate is considered. In Fig. 5,  $\theta_0/2$  is half of the corner angle, while  $R$  is the radius measured from the center of curvature to the reference neutral axis  $x$ . The length of the flange is  $l$ , and  $t$  is the thickness.

The analytical analysis assumes that the part undergoes two distinct types of deformation. The first type emerges during the curing cycle, leading to a shear deformation. Notably, in the early stages of the process, residual stresses are predominantly due to the transverse shear deformation. Therefore, the part experiences a negative deformation across its thickness. At the same time, the in-plane deformation is initially assumed to be negligible. The second deformation contribution emerges after the tool removal, when the part is detached from the tool, resulting in both spring-in and warpage angles. According to [23] and the previous considerations, the final spring-in angle can be expressed as

$$\phi_1 = \theta_s(x) - \gamma(x) = \begin{cases} -\frac{\varepsilon_2 x}{R} + \frac{\varepsilon_2}{aR} \cdot \frac{\cosh(al)}{\cosh\{a(R\theta_0/2+l)\}} \cdot \sinh(ax) & (0 \leq x \leq \frac{R\theta_0}{2}) \\ -\frac{\varepsilon_2 \theta_0}{2} + \frac{\varepsilon_2}{aR} \cdot \frac{\sinh(aR\theta_0/2)}{\cosh\{a(R\theta_0/2+l)\}} \cdot \sinh(a(R\theta_0/2+l-x)) & (\frac{R\theta_0}{2} \leq x \leq \frac{R\theta_0}{2} + l) \end{cases} \quad (12)$$

where  $\theta_s$  is the bending angle the part would experience without the tool,  $\gamma$  is the shear deformation,  $\varepsilon_2$  is the through-the-thickness strain. The parameter  $a$  is defined as:

$$a = \sqrt{\frac{10G_{\theta t}}{E_{\theta}t^2}} \quad (13)$$

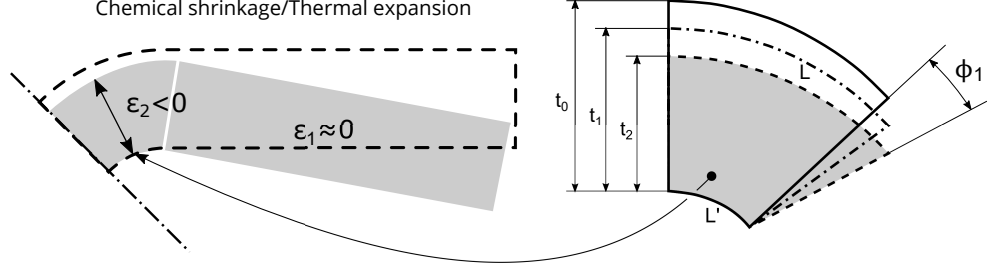


Figure 6: Deformation components due to chemical and thermal shrinkage along the part according to the closed-form solution.

where  $E_\theta$  and  $G_{\theta t}$  are the effective in-plane and out-of-plane moduli, respectively, with  $t$  denoting the thickness of the laminate. The angle is determined using two distinct expressions depending on which portion of the component is being studied. Specifically, the first row pertains to the curved section, while the second refers to the flange area. Figure 6 shows the effects shows the deformations according to the closed-form formulation, due to the chemical and thermal shrinkages. For a generic stacking sequence, the equivalent elastic matrix  $\mathbf{C}_{eq}$  has to be considered to evaluate the strain component vector  $\boldsymbol{\varepsilon}$  related to the laminate:

$$\mathbf{C}_{eq} = \frac{1}{N} \sum_{k=1}^N \mathbf{C}_k \quad (14)$$

where  $N$  is the number of layers. As seen above, the strain due to the application of the chemical and thermal load can be evaluated as follows:

$$\boldsymbol{\varepsilon}_{T+CH} = \boldsymbol{\alpha} \Delta T + \boldsymbol{\varepsilon}_S \quad (15)$$

The evaluation of  $\boldsymbol{\sigma}_{eq}$  can be obtained from:

$$\boldsymbol{\sigma}_{eq} = \frac{1}{N} \sum_{k=1}^N \boldsymbol{\sigma}_k = \frac{1}{N} \sum_{k=1}^N \mathbf{C}_k \boldsymbol{\varepsilon}_{T+S}^k \quad (16)$$

The equivalent deformation components for a composite part with  $N$  layers can be determined as follows:

$$\boldsymbol{\varepsilon} = \mathbf{S}_{eq} \boldsymbol{\sigma}_{eq} \quad (17)$$

where  $\mathbf{S}_{eq}$  is the equivalent compliance matrix. At each curing cycle's step, the cumulative spring-in angle is updated.

In the present analytical formulation, several assumptions are made. Firstly, the interface between the component and tool is frictionless, and equivalent material properties are used. The bending stiffness is not expected to change significantly, and thus, the bending properties adopted for each step are equal to the final value. Moreover, this formulation stage does not include the shear stress released by demolding. Finally, the in-plane deformation  $\varepsilon_1$  is considered negligible. The two assumptions regarding the bending and in-plane deformations make this model effective only for cross-ply laminates with equal layers at 0 and 90 degrees. This

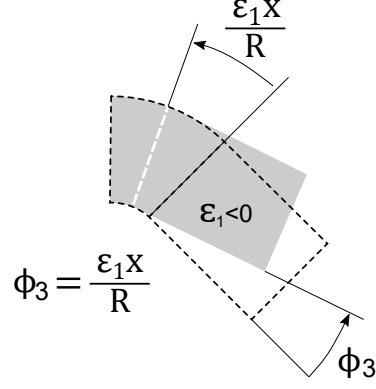


Figure 7: Effect of the in-plane strain component on the spring-in angle.

formulation can be enhanced and used for a generic balanced cross-ply laminate analysis by introducing two corrections. The initial effect pertains to the final demolding that may be included by scaling the deformation calculated at each step with the ratio between the current and the final bending modulus:

$$\phi_2 = \phi_{1t_i} \frac{E_{t_i}}{E_f} \quad (18)$$

where  $\phi_2$  is the updated spring-in angle and  $\phi_{1t_i}$  is the spring-in angle at k-th step. The second modification to be accounted for is the in-plane strain, denoted as  $\varepsilon_1$ . The integration of this component can be accomplished as follows:

$$\phi_3 = \begin{cases} \frac{\varepsilon_1 x}{R} & (0 \leq x \leq \frac{R\theta_0}{2}) \\ \frac{\varepsilon_1 \theta_0}{2} & (0 \leq x \leq \frac{R\theta_0}{2} + L) \end{cases} \quad (19)$$

where  $\theta_L$  is the updated spring-in angle, incorporating the effect for both the curved and the flat sections. Figure 7 shows the angle  $\phi_3$  resulting from the in-plane deformation. The modifications introduced enable the determination of the spring-in angle for composite parts composed of curved and flat parts. In this work, three analytical formulations will be employed. The first is the original formulation presented by [23]. The second accounts for the effect of the final demolding, while the third considers both the final demolding and the in-plane strain. Table 1 provides a summary of the three closed-form solutions discussed in this section, emphasizing the effects incorporated into the formulations, i.e.,

$$CF2 = CF1 + \text{Final demolding} \quad (20)$$

$$CF3 = CF2 + \text{In-plane strain} \quad (21)$$

Table 1: Summary of closed-form (CF) solutions and their respective contributions.

	Bending without tool	Warping with tool	Final demolding	In-plane strain	Spring-in angle
CF1	×	×			$\phi_1$
CF2	×	×	×		$\phi_2$
CF3	×	×	×	×	$\phi_2 + \phi_3$

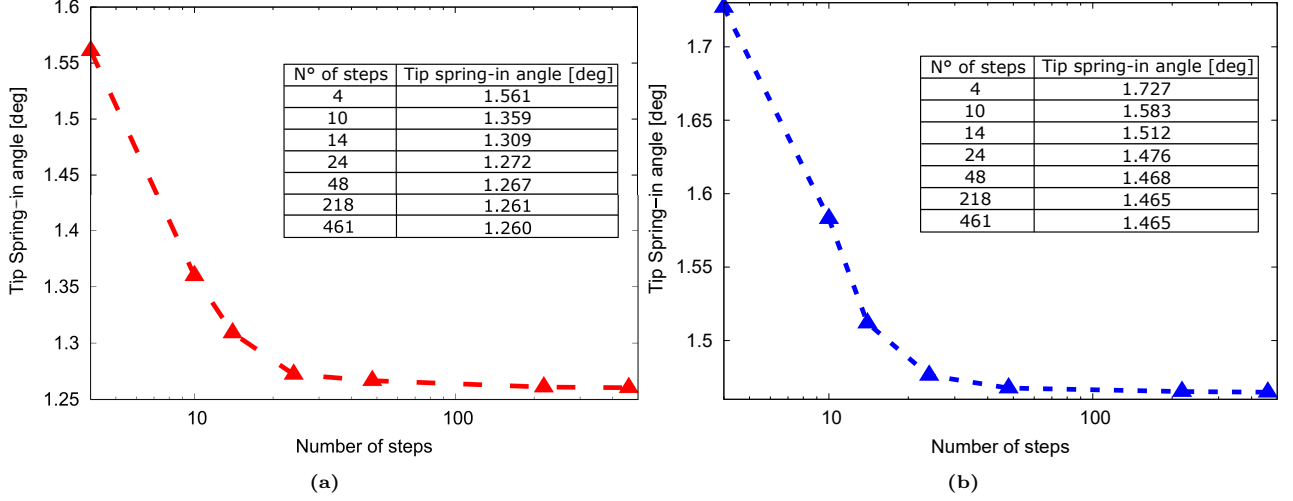


Figure 8: Convergence analysis for (a) numerical analysis with 242L9-1B4 mesh and (b) closed-form solution.

## 5 Assessment of the numerical model

The following section presents the results from the analytical approach, presented in Section 4, and the numerical models based on higher-order structural theories described in Section 2. Given the lack of results in the literature for a comprehensive combination of laminations, this section aims to study the deformations arising during the curing cycle of an L-shaped part and verify the numerical results with analytical ones, with a particular emphasis on the residual spring-in angle. Initially, a convergence analysis is conducted to determine the proper FE mesh, the structural modeling, and the number of steps for the curing simulation. By evaluating the resulting spring-in angles, the study seeks to identify the combination that provides the best trade-off of accuracy and computational efficiency. Then, the closed-form solution is employed to verify the numerical results by considering sixteen cross-ply stacking sequences.

### 5.1 Convergence analysis

The initial convergence analysis aims to define the number of analysis steps for the curing simulation. The number of steps is essential as the thermal and the elastic properties are updated at each time step, and the solution at the end of the process is the cumulative summation of the incremental solutions corresponding to each step [32]. The stacking sequence  $(90/0/90/0)_s$  was employed for the convergence analysis.

Figures 8a and 8b show the tip spring-in angle as the number of steps change. The analytical and numerical simulations consistently yield satisfactory results with 48 steps. For such a step size, the maximum variation of properties within one step is 5%; all the following analyses were carried out with 48 steps.

Table 2: Number of Degrees of Freedom (DOF) associated to each structural model.

N of DOF	
L4 - 1B4	3348
L4 - 2B4	5859
L9 - 1B4	12492
L9 - 2B4	21861
L16 - 1B4	27444
L16 - 2B4	48027

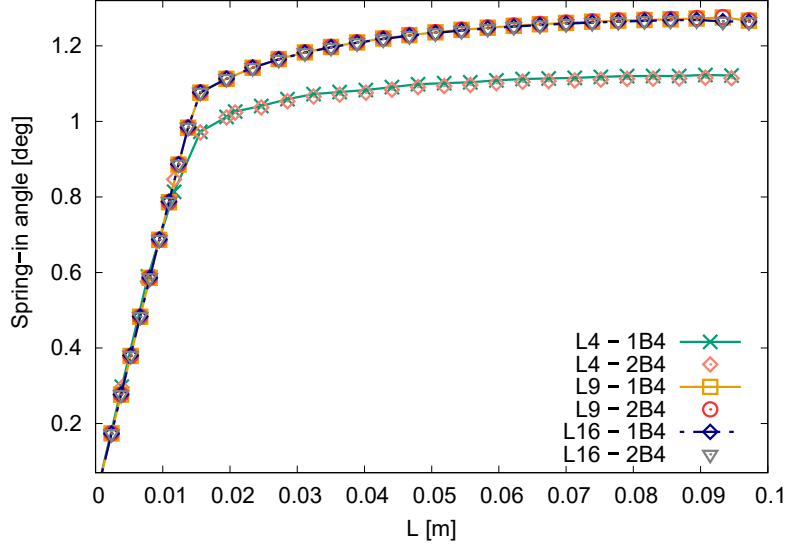


Figure 9: Convergence analysis for the structural model.

A convergence study is then conducted for the numerical model to determine the appropriate discretization along the beam direction and the structural modeling over the cross-section. The numerical model uses one-dimensional four-node B4 elements and bi-dimensional Lagrange elements - L4, L9, and L16 - for the cross-section. Table 2 reports the DOF associated to each structural model employed in the convergence analysis. The convergence results are shown in Fig. 9, where the variation of the spring-in angle is reported along the longitudinal direction of the model. The study reveals that L4 are less effective than L9 and L16 elements. However, using L16 elements does not significantly enhance accuracy compared to L9 elements, suggesting that L9 elements are adequate for this model. When calculating the spring-in angle, primarily occurring in the z-direction, using more one-dimensional elements is unnecessary. In every mesh, the number of Lagrange elements used in the cross-section is 242. Therefore, the 242L9 - 1B4 mesh, which balances computational efficiency and accuracy, is selected. Along z, one L9 per layer was used for the composite part, shear layer, and tool. Along x, eight L9 were used for the curved part, sixteen for the straight segment, and two for the final curve of the tool.

## 5.2 Comparison between numerical and closed-form solutions

This section analyzes the numerical and analytical outcomes regarding spring-in angles for the L-shaped model. First, the analytical findings for the  $(90/0/90/0)_s$  stacking sequence concerning the spring-in angle over the

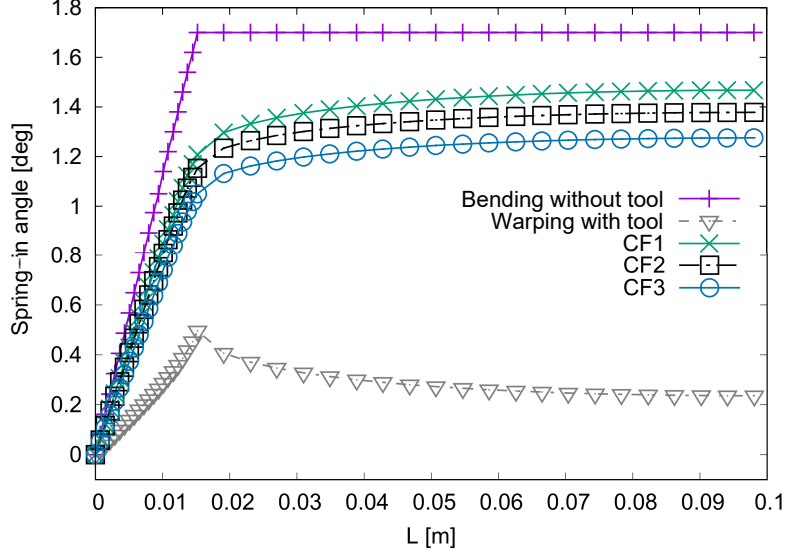


Figure 10: Comparison of closed-form solutions on the spring-in angle over the length of the part,  $(90/0/90/0)_s$ .

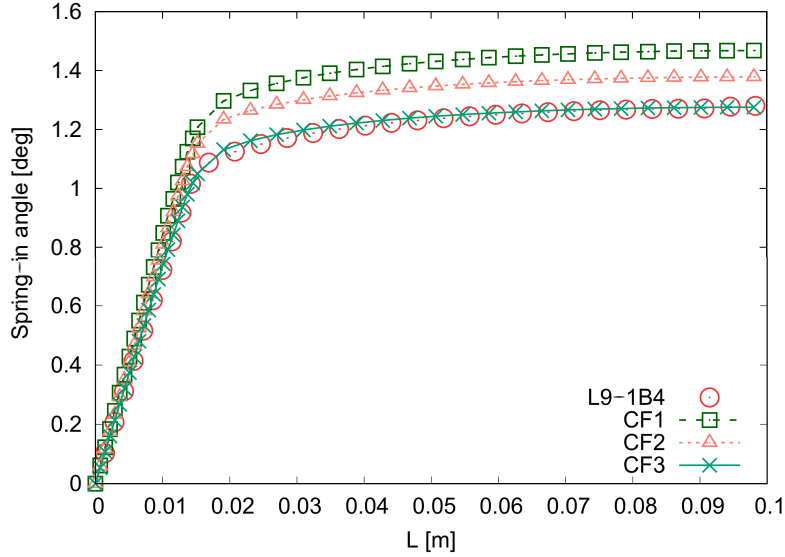


Figure 11: Comparison of numerical and analytical solutions on the spring-in angle over the length of the part,  $(90,0,90,0)_s$ .

length of the model are presented in Fig. 10. The figure shows the analytical contributions represented by the bending (purple line) and the warping (gray line) effects, which, when combined, yield the CF1 (Closed-Form 1) curve, shown in green. CF2 (black line) and CF3 (blue line) add the final demolding and in-plane strain effects, respectively; see Eqs. (20) and (21). Figure 11 compares the spring-in angles derived from analytical and numerical solutions along the length of the model. Table 3 presents the values of the tip spring-in angles and the relative percentage differences between the tip spring-in angles obtained from the numerical simulation and those derived from each closed-form solution:

$$\left| \frac{NS - CF^*}{CF^*} \right| \cdot 100 \quad (22)$$

Table 3: Tip spring-in angles for stacking sequence  $(90,0,90,0)_s$  and percentage difference of the numerical solution against the closed-form solutions (CF).

	Tip spring-in angle [deg]	relative difference [%]
Numerical solution	1.267	-
CF1	1.468	13.69%
CF2	1.378	8.05%
CF3	1.275	0.62%

Table 4: Symmetrical stacking sequences employed in the numerical assessment.

ID	LAM	Stacking sequence
1		$(0,0,0,90)_s$
2		$(0,0,90,0)_s$
3		$(0,90,0,0)_s$
4		$(90,0,0,0)_s$
5		$(0,0,90,90)_s$
6		$(0,90,0,90)_s$
7		$(0,90,90,0)_s$
8		$(90,0,0,90)_s$
9		$(90,0,90,0)_s$
10		$(90,90,0,0)_s$
11		$(0,90,90,90)_s$
12		$(90,0,90,90)_s$
13		$(90,90,0,90)_s$
14		$(90,90,90,0)_s$
15		$(0,0,0,0)_s$
16		$(90,90,90,90)_s$

where NS represents the tip spring-in angle values obtained from numerical simulations, as indicated in the first row of Table 3, CF\* refers to the specific closed-form solution, e.g., in the second row of Table 3, 13.69% indicates the relative percentage difference between the tip spring-in angle calculated numerically (NS) and that derived from the first closed-form solution (CF1). The results suggest that

- CF1 presents higher values while introducing the demolding effect (CF2) results in a lower spring-in angle. Furthermore, adding in-plane deformation in CF3 further reduces the final angle.
- A good match between the spring-in angles from analytical and numerical solutions is observed using CF3, including the final demolding and the in-plane strain effects.

The last assessment in this section considers the symmetric stacking sequences in Table 4. The outcomes of the model's tip spring-in angles for all the stacking sequences are shown in Fig. 12. The tip spring-in angle is calculated with CF1, CF2, CF3, and the numerical solution; the following comments can be made:

- For sequences 1 to 4, which primarily feature  $0^\circ$  orientations, the differences between CF solutions are not negligible but less significant compared to the balanced stacking sequences from 5 to 10.
- Sequences 11 to 14 have more  $90^\circ$  orientations and high differences between CF solutions.
- Sequence 15 has all three CF very close and matching numerical results.



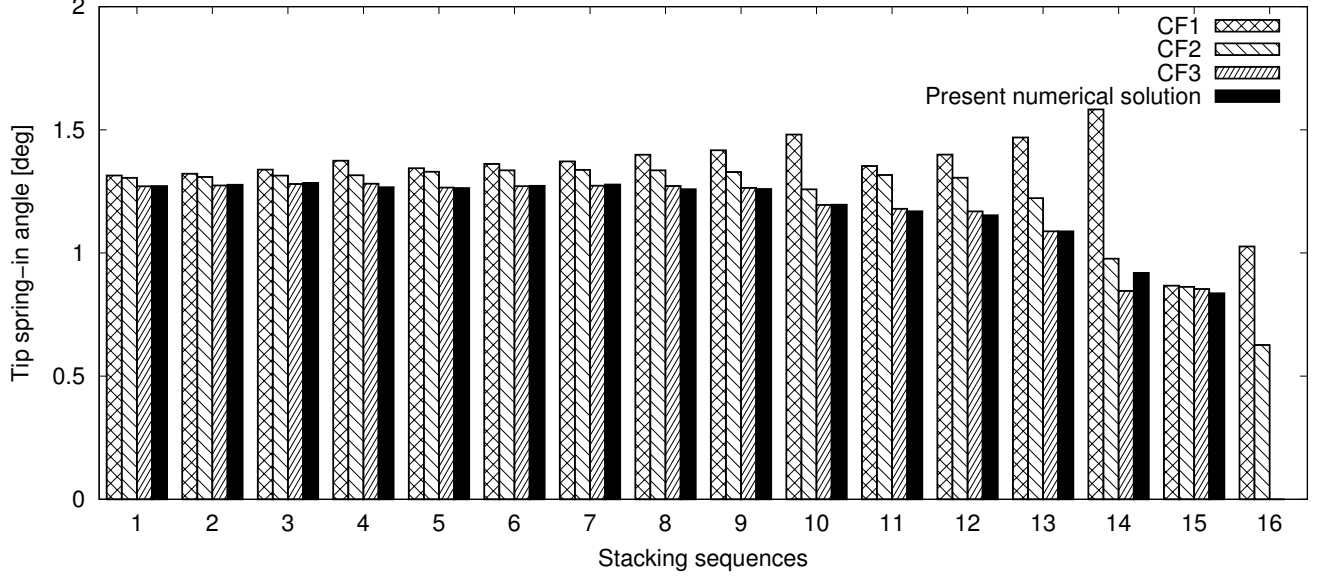


Figure 12: Comparison of tip spring-in angles for symmetric stacking sequences from analytical and numerical simulations. For stacking sequence 16:  $CF1 = 1.0265^\circ$ ,  $CF2 = 0.6264^\circ$ ,  $CF3 = 0.0^\circ$ , Present numerical solution =  $-4.9054E-05^\circ$ .

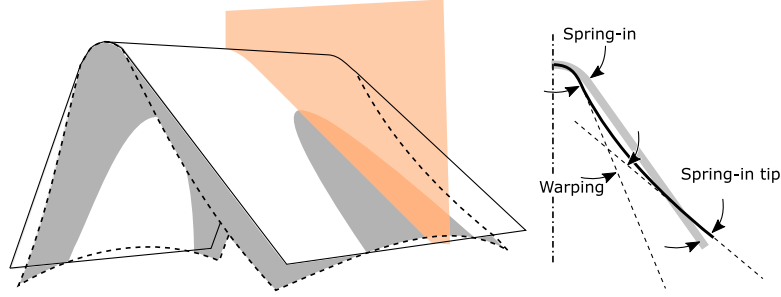


Figure 13: Warping and spring-in angle locations along the cross-section.

- When all layers have the  $90^\circ$  orientation, stacking 16,  $CF1$  and  $CF2$  are very far from  $CF3$  and the numerical results.
- The effect of final demolding and in-plane deformation is more relevant when  $90^\circ$  orientations are used.

## 6 Numerical results and mitigation strategies

This section employs the previously introduced and verified numerical simulation for conducting a parametric analysis. The effect of the stacking sequence is analyzed by considering all the possible combinations ( $2^8 = 256$ ) of an eight-layer cross-ply L-shaped laminate. The results consider warping and spring-in angles as shown in Fig. 13. Then, a mitigation strategy for reducing spring-in angles is investigated.

### 6.1 Symmetrical and asymmetric stacking sequences

The two sections considered are shown in Fig. 14. The first section is at  $y=0$  - section A - and the second is at the model's mid-span - section B. Figure 14 shows warping and spring-in angles in section B. The size of the

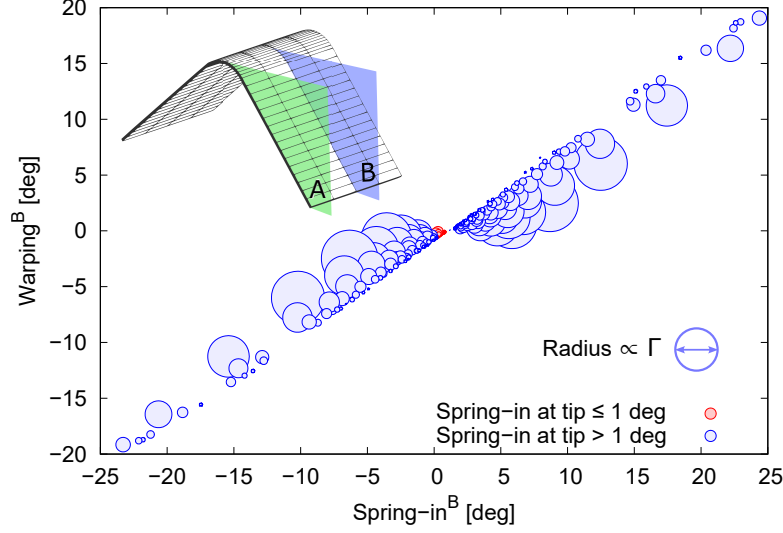


Figure 14: Warping and spring-in angles in section B.  $\Gamma$  is the longitudinal warping.

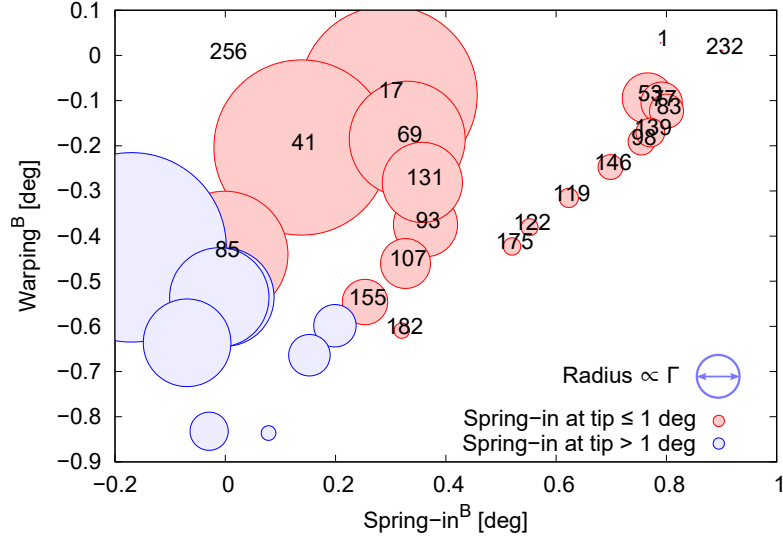


Figure 15: Laminations with low residual deformations.

circles is proportional to the longitudinal warping  $\Gamma$ ; see Fig. 1. In Fig. 15, the laminations having deformations approaching zero are shown, and Table 5 reports the stacking sequences and the values of the angles. Laminations with a spring-in tip smaller than one were considered: the 91 lamination is the reference considered in previous sections. Figure 16 illustrates the relationship between warping and spring-in angle, distinguishing between symmetric and asymmetric laminations. Consistent with expectations, symmetric stacking sequences yield lower spring-in and warping angles. However, it is observed that the best performance in minimizing these deformations is achieved with asymmetric laminates. Table 5 reports the deformations of those stacking sequences that exhibit minimum spring-in angles. For instance, 0/90/90/0/90/90/90/0 exhibits the lowest tip spring-in angle.

Table 5: Stacking sequences with low residual deformations. The angles are expressed in deg.

ID LAM	Stacking sequences	Spring-in tip	Spring-in B	Spring-in A	Warping B	Warping A
91	0/90/0/90/90/0/90/0	1.27	1.17	1.17	0.06	0.06
98	90/0/0/0/0/90/90/0	0.32	0.75	1.08	-0.19	-0.35
119	0/90/90/0/90/90/90/0	-0.06	0.62	0.86	-0.32	-0.42
122	90/0/0/90/90/90/90/0	-0.27	0.55	0.76	-0.38	-0.48
139	0/90/0/90/0/0/0/90	0.39	0.77	1.13	-0.17	-0.33
146	90/0/0/0/90/0/0/90	0.15	0.7	1	-0.25	-0.4
175	0/90/90/90/0/90/0/90	-0.39	0.52	0.73	-0.42	-0.53
182	90/0/90/0/90/90/0/90	-0.99	0.32	0.5	-0.61	-0.71
232	90/90/90/0/0/90/90/90	0.92	-0.9	-0.9	0.01	0.01

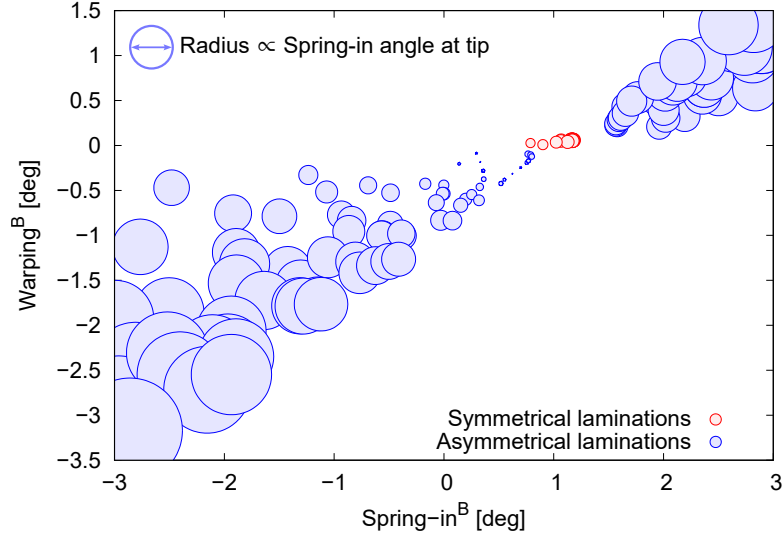


Figure 16: Distribution of symmetric and asymmetric laminations in warping against spring-in angle.

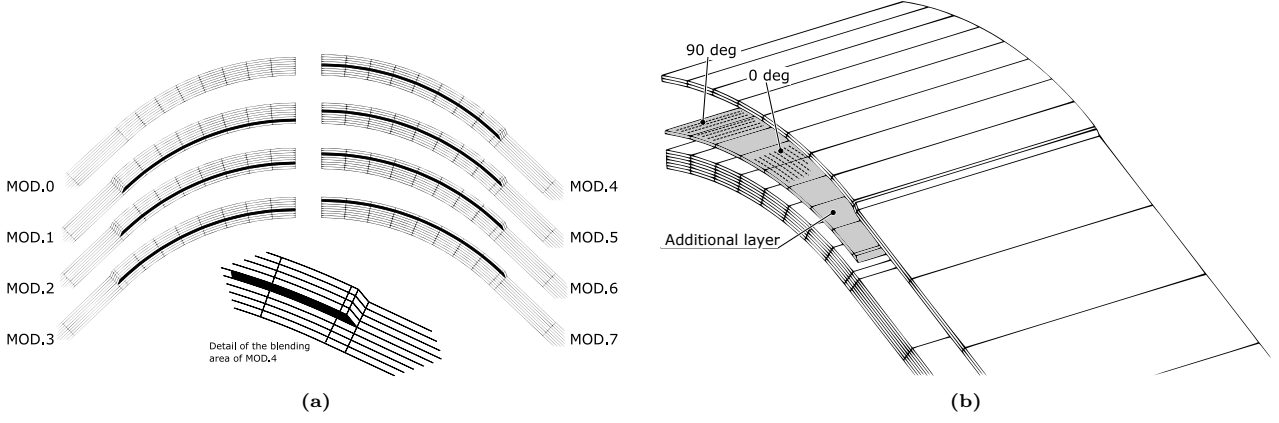


Figure 17: (a) Patch locations. (b) Detail on the insertion of the additional layer.

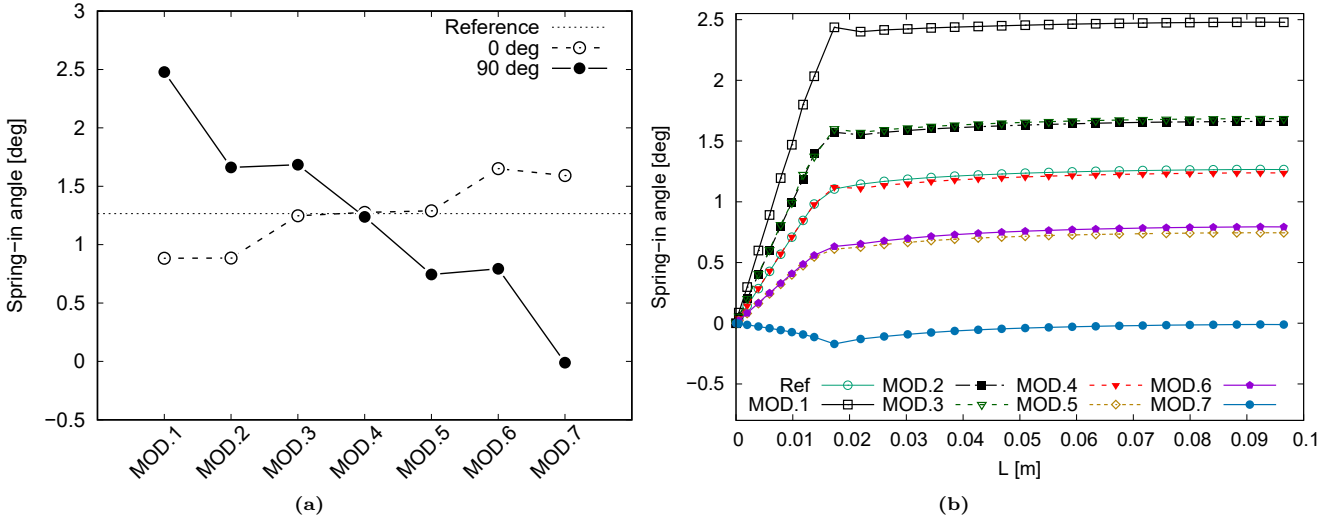


Figure 18: (a) Effect of the lamination angle of the patch on the spring-in angle. (b) Spring-in angle along the length for 90° patches.

## 6.2 Spring-in angle mitigation through localized composite patches

According to the results shown in the previous section, while symmetric laminations tend to have smaller spring-in angles, the most effective minimization is achievable with asymmetric stacking sequences. However, the latter may be challenging due to undesirable coupling effects. The present section explores an alternative solution, i.e., introducing localized composite patches over the curved part. Patches unbalance laminations locally, and this may neutralize the spring-in angle. The optimal placement and design of the patches aim to minimize spring-in angle and coupling effects.

Firstly, the investigation will focus on the effects of incorporating an additional layer, made of the same material as the laminate, into a symmetric stacking sequence. The layer is placed in various corner positions, and seven configurations were considered, as shown in Fig. 17a. Furthermore, the influence of the patch orientation angle - 90° or 0° - is investigated, as shown in Fig. 17b.

Figure 18a shows the tip spring-in angle for the different patch configurations. The reference is the value without patches. The most significant reduction in spring-in value is given by MOD.1 with a 0° layer, while for the 90°

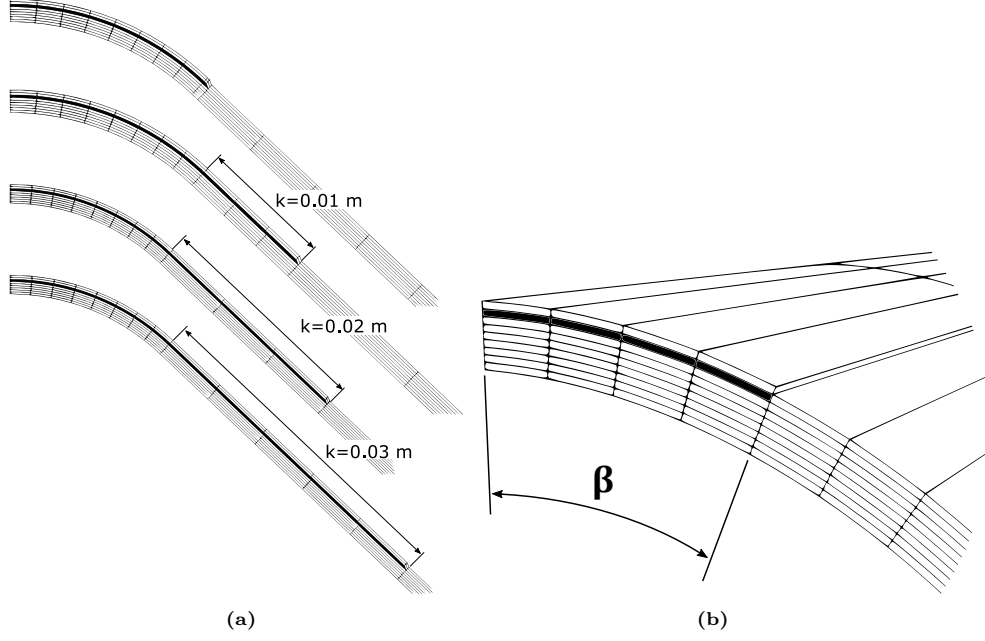


Figure 19: (a) Models with different lengths of the patch. (b) Angle covered by the patch.

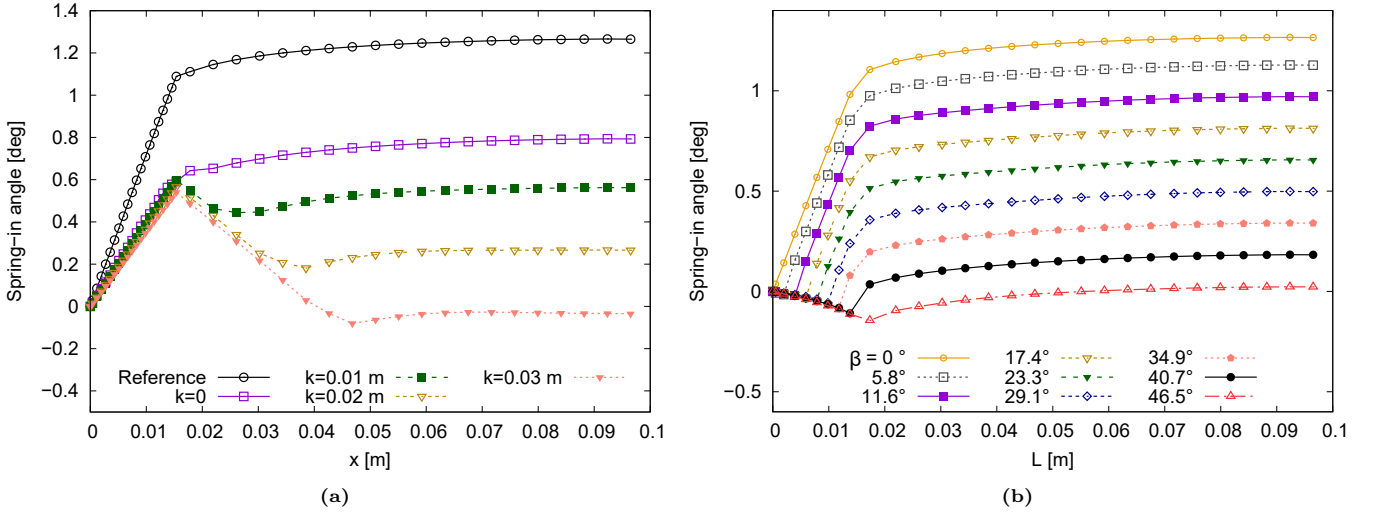


Figure 20: Spring-in angle of MOD.6 and  $90^\circ$  lamination patch for (a) different values of  $k$  and (b) different values of  $\beta$ .

layer, the most substantial reduction is given by MOD.7. The latter can reduce the spring-in angle from about  $1.3^\circ$  to almost  $0^\circ$ . Figure 18b shows each configuration's spring-in angle along the x-coordinate. The results indicate that MOD.7 effectively reduces the spring-in angle along the entire flange to nearly  $0^\circ$ , with marginally negative values on the curved part.

The reduction in residual deformations is also influenced by the patch geometry. Figure 19a shows different patch lengths,  $k$ , while Fig. 19b shows a patch partially covering the corner.

Figure 20a shows that, as the value of  $k$  increases, the spring-in angle along the flange decreases. However, the angle achieved in the curved part by all the  $k$  configurations remains equivalent to  $k=0$ . Conversely, Fig. 20b shows the results when the angle  $\phi$  increases. In this scenario, both the curved and flat parts of the model are influenced by the angle covered by the patch. Overall, it is observed that the lowest spring-in angle is obtainable

with the complete coverage of the curved part.

## 7 Discussion

The initial analysis evaluated the accuracy of spring-in angles derived from the present numerical analysis for an L-shaped model by comparisons with closed-form solutions. The analytical results for the stacking sequence  $(90/0/90/0)_s$  were first calculated using the original closed-form solution by Takagaki [23], denoted as CF1, which considers the effects of bending and warping. Subsequently, a second solution, CF2, extended the CF1 by incorporating the demolding effect. A third solution, CF3, builds upon CF2 by adding the in-plane strain effects; see Fig. 10. These progressive modifications to CF1 are intended as corrective adjustments and significantly influence the spring-in angles, with CF3 matching the numerical solution. The enhancement of the closed-form solutions led to smaller spring-in angles.

The second set of results focused on the effect of the stacking sequence on warping and spring-in angles. All combinations - 256 - of an eight-layer cross-ply laminate were considered. Warping and spring-in angles were computed in model sections, as shown in Fig. 14. The findings have indicated the superior performance of asymmetric models in reducing the deformations associated with warping and spring-in angles, as illustrated in Fig. 16. Table 5 shows the best stacking sequences. LAM 119  $(0/90/90/0/90/90/90/0)$  reduced the tip spring-in angle to  $-0.06^\circ$ . Moreover, LAM 182  $(90/0/90/0/90/90/0/90)$  reduced the spring-in angle in Section A to  $0.5^\circ$  and to  $0.32^\circ$  in Section B. While LAM 232  $(90/90/90/0/0/90/90/90)$  reduced the warping in Sections A and B to  $0.01^\circ$ .

The outcomes from Section 6.1 confirmed that symmetric laminations typically ensure lower deformations. However, the coupling introduced by asymmetric laminations can be exploited to counterbalance undesirable deformations. Consequently, a mitigation strategy was proposed using localized patches to induce an unbalanced effect, reducing the overall deformation. Figure 18 indicates that an additional  $90^\circ$  layer covering the entire corner affects the spring-in angle significantly, reducing it from a reference value of circa  $1.2^\circ$  to nearly  $0^\circ$ . Extending the patch to the flat part of the structure predominantly impacts the spring-in angle outside the curved area, leading to negligible values when  $k=0.03$  m, as shown in Fig. 20a.

## 8 Conclusions

This paper investigates the residual deformations — spring-in and warping angles — of an L-shaped composite part after the curing cycle and proposes mitigation strategies to minimize such deformations. The analysis has employed a 1D layer-wise numerical model based on the Carrera Unified Formulation (CUF) and the Cure-Hardening Instantaneously Linear Elastic constitutive model. The numerical simulation's accuracy has been evaluated through a closed-form solution. The results suggest that:

- A good match between numerical and analytical formulations was found. The inclusion of in-plane strain and demolding effects in the closed-form solution proved to be effective.
- Asymmetric laminates offer a broader spectrum of residual deformations than symmetric configurations. Furthermore, asymmetric sequences can potentially reduce residual deformations significantly.
- Applying localized patches in the curved section of composite parts can reduce deformations significantly, too.

Future research should consider the analysis of residual stresses throughout the thickness of the laminate. Furthermore, additional physical phenomena should be integrated, such as the tool-part interaction and the pressure cycle inside the autoclave. The use of different materials for the patches with different thermal expansion values will be investigated. Furthermore, the scope of research will be expanded to include various composite shapes that hold significance in the aerospace industry, broadening the applicability and relevance of the study's findings.

## Acknowledgements

This work was partly supported by the Italian Ministry of Foreign Affairs and International Cooperation (grant number US23GR12).

## References

- [1] G. Fernlund, C. Mobuchon, and N. Zobeiry. Autoclave Processing. *Reference Module in Materials Science and Materials Engineering*, 12 2017.
- [2] N. Zobeiry and A. Poursartip. The origins of residual stress and its evaluation in composite materials. In P. W. R. Beaumont, C. Soutis, and A. Hodzic, editors, *Structural Integrity and Durability of Advanced Composites*, Woodhead Publishing Series in Composites Science and Engineering, pages 43–72. Woodhead Publishing, 2015.
- [3] S. Chava and S. Namilae. Continuous evolution of processing induced residual stresses in composites: An in-situ approach. *Composites Part A: Applied Science and Manufacturing*, 145:106368, 2021.
- [4] P.H. Shah, V. A. Halls, J.Q. Zheng, and R. C. Batra. Optimal cure cycle parameters for minimizing residual stresses in fiber-reinforced polymer composite laminates. *Journal of Composite Materials*, 52(6):773–792, 2018.
- [5] M. H. Nagaraj and M. Maiaru. Micro-scale process modeling and residual stress prediction in fiber-reinforced polymers using refined structural models. Proceedings for the American Society for Composites-Thirty Seventh Technical Conference, 2022.
- [6] Q. T. L. Vu, G. Seon, S. Ghaffari, A. Makeev, F. Lachaud, M. Charlotte, and Y. Gourinat. Evaluating Residual Stress in Carbon Fiber-Reinforced Polymer (CFRP) at Microscale Using Fiber Push-Out Experiment and Finite Element Modeling. *Polymers*, 15(12), 2023.
- [7] S. Zhang, Y. Xu, and W. Zhang. A novel micromechanical model to study the influence of cure process on the in-plane tensile properties of z-pinned laminates. *Composite Structures*, 300:116156, 2022.
- [8] B. Wang, S. Fan, J. Chen, W. Yang, W. Liu, and Y. Li. A review on prediction and control of curing process-induced deformation of continuous fiber-reinforced thermosetting composite structures. *Composites Part A: Applied Science and Manufacturing*, 165:107321, 2023.
- [9] N. Traiforos, M. Matveev, D. Chronopoulos, and T. Turner. Spring-in of composite L-shape specimens: An experimental and numerical investigation. *Composite Structures*, 310:116772, 2023.
- [10] M. N. M. Nasir, M. A. Seman, L. Mezeix, Y. Aminanda, A. Rivai, and K. M. Ali. Effect of Stacking Layup on Spring-back Deformation of Symmetrical Flat Laminate Composites Manufactured through Autoclave Processing. volume 184, page 012028. IOP Publishing, mar 2017.
- [11] D.-H. Kim and S.-W. Kim. Process-induced distortion of triaxially braided composites considering different geometric parameters using simplified constitutive model with effective property. *Finite Elements in Analysis and Design*, 222:103974, 2023.



- [12] G. Fernlund, A. Poursartip, G. Twigg, and A. Carolyne. Residual Stress, Spring-In and Warpage in Autoclaved Composite Parts. Proceedings of 14th International Conference on Composite Materials, 2003.
- [13] D. W. Radford and T. S. Rennick. Separating Sources of Manufacturing Distortion in Laminated Composites. *Journal of Reinforced Plastics and Composites*, 19(8):621–641, 2000.
- [14] G. Fernlund and A. Floyd. Process analysis and tool compensation for a complex composite panel. volume 2. American Society for Composites 22nd Annual Technical Conference, Seattle, 01 2007.
- [15] L. Sorrentino and C. Bellini. Compaction influence on spring-in of thin composite parts: Experimental and numerical results. *Journal of Composite Materials*, 49(17):2149–2158, 2015.
- [16] G. Zhang, J. Wang, A. Ni, H. Hu, A. Ding, and S. Li. Process-induced deformation of L-shaped variable-stiffness composite structures during cure. *Composite Structures*, 230:111461, 2019.
- [17] Y. Zhou, M. Li, Q. Cheng, S. Wang, Y. Gu, and X. Chen. Quantitative relations between curing processes and local properties within thick composites based on simulation and machine learning. *Materials & Design*, 226:111686, 2023.
- [18] C. Schoenholz, S. Li, K. Bainbridge, V. Huynh, A. Gray, and N. Zobeiry. Accelerated In Situ Inspection of Release Coating and Tool Surface Condition in Composites Manufacturing Using Global Mapping, Sparse Sensing, and Machine Learning. *Journal of Manufacturing and Materials Processing*, 7:81, 04 2023.
- [19] S. Fan, J. Zhang, B. Wang, J. Chen, W. Yang, W. Liu, and Y. Li. A deep learning method for fast predicting curing process-induced deformation of aeronautical composite structures. *Composites Science and Technology*, 232:109844, 2023.
- [20] M. R. Wisnom, K. Potter, and N. Ersoy. Shear-lag Analysis of the Effect of Thickness on Spring-in of Curved Composites. *Journal of Composite Materials*, 41(11):1311–1324, 2007.
- [21] A. Ding, J. Wang, A. Ni, and S. Li. A new analytical solution for cure-induced spring-in of L-shaped composite parts. *Composites Science and Technology*, 171:1–12, 2019.
- [22] X. Peng, J. Xu, Y. Cheng, L. Zhang, J. Yang, and Y. Li. An Analytical Model for Cure-Induced Deformation of Composite Laminates. *Polymers*, 14(14), 2022.
- [23] K. Takagaki, S. Minakuchi, and N. Takeda. Process-induced strain and distortion in curved composites. Part I: Development of fiber-optic strain monitoring technique and analytical methods. *Composites Part A: Applied Science and Manufacturing*, 103:236–251, 2017.
- [24] A. Balaji, C. Sbarufatti, D. Dumas, A. Parmentier, O. Pierard, and F. Cadini. Prediction of shape distortions in thermosetting composite parts using neural network interfaced visco-elastic constitutive model. *Journal of Composite Materials*, 2024.

- [25] Z. Liu, X. Zheng, W. Fan, F. Wang, S. Ahmed, and L. Yan. An alternative method to reduce process-induced deformation of cfrp by introducing prestresses. *Chinese Journal of Aeronautics*, 35(8):314–323, 2022.
- [26] B. Wucher, Ph. Martiny, F. Lani, T. Pardoen, C. Bailly, and D. Dumas. Simulation-driven mold compensation strategy for composites: Experimental validation on a doubly-curved part. *Composites Part A: Applied Science and Manufacturing*, 102:96–107, 2017.
- [27] E. Carrera, M. Cinefra, M. Petrolo, and E. Zappino. *Finite Element Analysis of Structures through Unified Formulation*. John Wiley and Sons, Ltd, Hoboken, New Jersey, USA, 2014.
- [28] E. Carrera and E. Zappino. One-dimensional finite element formulation with node-dependent kinematics. *Computers & Structures*, 192:114–125, 2017.
- [29] D. Scano, E. Carrera, and M. Petrolo. Use of the 3d equilibrium equations in the free-edge analyses for laminated structures with the variable kinematics approach. *Aerotecnica Missili e Spazio*, 2023.
- [30] L. Qi, M.H. Nagaraj, E. Carrera, C.F. Gao, and M. Petrolo. Numerical analysis of disbonding in sandwich structures using 1d finite elements. *Composite Structures*, 252:112717, 2020.
- [31] E. Zappino, N. Zobeiry, M. Petrolo, R. Vaziri, E. Carrera, and A. Poursartip. Computationally Efficient Thermo-Mechanical Analysis for Predicting Process-Induced Deformations of Composite Structures. Volume 2A: Advanced Manufacturing, 11 2019.
- [32] E. Zappino, N. Zobeiry, M. Petrolo, R. Vaziri, E. Carrera, and A. Poursartip. Analysis of process-induced deformations and residual stresses in curved composite parts considering transverse shear stress and thickness stretching. *Composite Structures*, 241:112057, 2020.
- [33] A. Pagani, M. Enea, and E. Carrera. Quasi-static fracture analysis by coupled three-dimensional peridynamics and high order one-dimensional finite elements based on local elasticity. *International Journal for Numerical Methods in Engineering*, 123, 11 2021.
- [34] A. G. de Miguel, A. Pagani, L. Rizzo, A. Catapano, and E. Panettieri. Accurate evaluation of 3D stress fields in adhesive bonded joints via higher-order FE models. *Mechanics of Advanced Materials and Structures*, 27(4):333–345, 2020.
- [35] A. Johnston, R. Vaziri, and A. Poursartip. A Plane Strain Model for Process-Induced Deformation of Laminated Composite Structures. *Journal of Composite Materials*, 35(16):1435–1469, 2001.
- [36] X. Zeng and J. Raghavan. Role of tool-part interaction in process-induced warpage of autoclave-manufactured composite structures. *Composites: Part A*, 2010.
- [37] *Hexcel, HexPly 8552 product data sheet*, 2016.

- [38] *Hexcel, HexTow AS4 product data sheet.*
- [39] D. Van Ee and A. Poursartip. *HexPly 8552 MATERIAL PROPERTIES DATABASE for use with COMPRO CCA and Raven.* National Center for Advanced Materials Performance, Wichita, KS, 2009.
- [40] A. Shahkarami, D. Van Ee, and A. Poursartip. *Material Characterization for Processing: Hexcel 8552.* National Center for Advanced Materials Performance, Wichita, KS, 2009.
- [41] *Convergent Manufacturing Technologies, RAVEN simulation software.*
- [42] C. Mobuchon, N. Zobeiry, C. Duffner, and A. Poursartip. A Multifaceted Approach for Process Characterization of Polymer-matrix Composites. 07 2018.
- [43] M. R. Wisnom, K. D. Potter, and N. Ersoy. Shear-lag Analysis of the Effect of Thickness on Spring-in of Curved Composites. *Journal of Composite Materials*, 41(11):1311–1324, 2007.